



Out-of-phase thermomechanical fatigue crack propagation in a steam turbine steel — Modelling of crack closure

Ahmed Azeez^{a,*}, Viktor Norman^b, Robert Eriksson^a, Daniel Leidermark^a, Johan Moverare^b

^a Division of Solid Mechanics, Department of Management and Engineering, Linköping University, SE-581 83 Linköping, Sweden

^b Division of Engineering Materials, Department of Management and Engineering, Linköping University, SE-581 83 Linköping, Sweden

ARTICLE INFO

Keywords:

Thermomechanical fatigue
Fatigue crack growth
High temperature steel
Crack closure
Numerical modelling

ABSTRACT

Understanding of crack growth behaviour is necessary to predict accurate fatigue lives. Out-of-phase thermomechanical fatigue crack propagation tests were performed on FB2 steel used in high-temperature steam turbine sections. Testing results showed crack closure where the compressive part of the fatigue cycle affected crack growth rate. Crack closing stress was observed to be different, and had more influence on the growth rate, than crack opening stress. Crack growth rate was largely controlled by the minimum temperature of the cycle, which agreed with an isothermal crack propagation test. Finite element models with stationary sharp cracks captured the crack closure behaviour.

1. Introduction

As power production turbines to a greater extent supports renewable energies, the turbines are required to manage flexible operation with faster loading ramps [1,2]. This flexibility is needed due to the intermittent nature of renewable energy sources, which is influenced by the change in weather. For steam turbines, the frequent start-ups with fast ramping rates put several components under large thermal stresses due to temperature gradients, especially in thick-walled components at the high- and intermediate-pressure turbine sections [1,3].

Under such loading conditions, i.e. thermomechanical fatigue (TMF) loading, the turbine component's life need to be determined with accurate and less conservative fatigue life prediction models to allow for more start-ups. This is done by letting the components operate closer to their end of life, i.e. passing the crack initiation phase and allowing crack growth. The controlled growth of cracks provide a useful tool to extend operation and avoid unnecessary waste of resources within safe limits. This particularly emphasises the need for crack propagation models. Thus, testing and modelling of TMF crack propagation have arisen as important fields of research in the turbine sector. The choice of TMF cycle type, i.e. how the temperature vary along with the load, depends mainly on the target component being investigated. In the current work, the main focus is on the inner section of the steam turbine casing, where an out-of-phase (OP) type of TMF loading is present.

Isothermal fatigue crack growth testing is widely used as it has a well

established and less complicated testing procedure as well as less complicated data post-processing methods compared to TMF crack growth testing. Nevertheless, TMF crack growth testing has emerged as an important topic when studying critical components. Thus, several researches have been focusing on investigating and laying guidelines for TMF crack propagation testing [4–6].

In studies done on nickel-based polycrystalline alloys, several TMF crack propagation tests showed clear dependency on crack closure [7]. By compensating for crack closure using an effective stress intensity range [8], OP-TMF tests with different load ratios fell onto a single master curve [9,10]. Furthermore, OP-TMF crack growth curves were seen to collapse on isothermal tests done at temperature close to the minimum temperature of the OP-TMF cycle, which was explained by plasticity induced crack closure [10]. Similarly, crack growth curves for titanium alloys tested under OP-TMF conditions collapsed on isothermal test done at the minimum temperature of the OP-TMF cycle [11]. Crack growth investigation done on single-crystal nickel-based alloys under OP-TMF conditions showed a different behaviour after correcting for crack closure compared to isothermal crack growth tests [12]. This was explained by the different thermal exposure histories between the two types of tests. Interestingly though, the OP-TMF crack propagation rates were not affected by different maximum temperatures used in the tests [12].

Regarding crack closure, the contribution from the compressive part of the cycle has been observed to affect the crack growth behaviour due

* Corresponding author.

E-mail address: ahmed.azeez@liu.se (A. Azeez).

<https://doi.org/10.1016/j.ijfatigue.2021.106251>

Received 13 December 2020; Received in revised form 15 February 2021; Accepted 19 March 2021

Available online 25 March 2021

0142-1123/© 2021 The Author(s). Published by Elsevier Ltd. This is an open access article under the CC BY license (<http://creativecommons.org/licenses/by/4.0/>).

to the crack not being completely closed [13]. Crack opening stress, when the crack becomes fully open during loading, has usually been used to account for the closure effects. Nevertheless, crack closing stress, when the crack starts to close during unloading, has been observed to differ and normally be lower than the crack opening stress [14]. The difference between crack opening and crack closing stresses increases with the increase in the maximum stress of the cycle which is explained by the large reversed plasticity required to close the crack [14]. Residual stresses due to plasticity in the first half cycle has been used to provide a sufficient load ratio correction [15]. It has also been shown that linear elastic fracture mechanics (LEFM) could still be satisfactorily applied to hysteresis loops slightly deviating from linear elastic behaviour (i.e. where some minor degree of plasticity occurred) [15].

In the current work, OP-TMF crack propagation testing was performed under stress and strain control for various stress and strain ranges. The crack growth behaviour was investigated to understand the effect of loading ratio on crack growth. In addition, an isothermal crack propagation test was performed at a temperature corresponding to the minimum temperature in the OP-TMF cycle. Crack closure was accounted for both experimentally and by finite element (FE) modelling in an attempt to arrive at a single master crack propagation curve for all thermomechanical loading conditions.

2. Material and experiments

2.1. Material

The material used in this work is FB2 steel (9Cr-1Mo-1Co-0.2 V-0.07Nb-0.01B-0.02 N, all in wt%). The material was subjected to a heat treatment consisting of austenitisation at 1100 °C with rapid cooling followed by two stages of tempering at 570 °C and 710 °C [16]. A microstructure study of FB2, by [17], revealed that the microstructure was tempered martensite. This steel belongs to the 9–12 % Cr steel class and can be used in structural components up to around 625 °C [18–20]. The development of FB2 was done within the European Cooperation in Science and Technology (COST) 522 program (1998–2003) [16,18]. The creep and steam oxidation resistance of this material at high temperature has made it favourable for usage in the steam turbine components operating in ultra-super critical steam conditions [18,21]. Although FB2 steel is intended for use in components produced by forging (such as rotors [20]), this study uses TMF conditions from the casing (which is produced by casting). This to avoid the trouble of testing coarse-grained alloys.

2.2. Isothermal fatigue crack propagation

Isothermal fatigue crack propagation testing was performed at 100 °C using a compact tension (CT) specimen. The specimen had an effective width, W , of 25 mm and thickness, B , of 12.5 mm with a manufactured crack starter of length $a = 11$ mm, as shown in Fig. 1. After machining and drilling of holes, the detailed profile of the CT specimen, with the manufactured crack starter, was made using electrical discharge machining (EDM) without application of additional surface finishing processes. The specimen was pre-cracked at room temperature to an initial crack length of about $a = 12.5$ mm and further tested at elevated temperature (100 °C) using a load range of 4500 N and a load ratio $R = F_{\min}/F_{\max} = 0.05$; F_{\min} and F_{\max} being the minimum and maximum load during the cycle. A trapezoidal waveform was chosen with a ten second ramp-up, a one second hold at maximum load, followed by a ten second ramp-down and a one second hold at minimum load. The testing was performed in a 100 kN Alwetron electro-mechanical test frame equipped with an external digital controller 580 V from Doli and a 3-zone split furnace.

Crack lengths, a , were measured using a pulsed direct-current potential drop system from Matelect using a current of 5 A pulsed with a frequency of 1 Hz. The determination of a from voltage for CT specimen was done following Ref. [22]. The crack propagation was assessed based on LEFM, where the equations for the stress intensity factor, K , can be readily found in various handbooks or standards, e.g. Ref. [23],

$$K = \frac{F}{B\sqrt{W}} f_{\text{CT}}\left(\frac{a}{W}\right) \quad (1)$$

where F is the applied load, B and W are specimen dimensions (see Fig. 1), and f_{CT} is the stress intensity factor function for CT specimen given by

$$f_{\text{CT}}\left(\frac{a}{W}\right) = \frac{\left(2 + \frac{a}{W}\right)}{\left(1 - \frac{a}{W}\right)^{3/2}} \left(0.886 + 4.64\left(\frac{a}{W}\right) - 13.32\left(\frac{a}{W}\right)^2 + 14.72\left(\frac{a}{W}\right)^3 - 5.6\left(\frac{a}{W}\right)^4\right) \quad (2)$$

with a being the crack length measured from the load line, see Fig. 1.

2.3. Thermomechanical fatigue crack propagation

Crack propagation tests under TMF conditions involve subjecting cracked specimens to both cyclic load and cyclic temperature. The

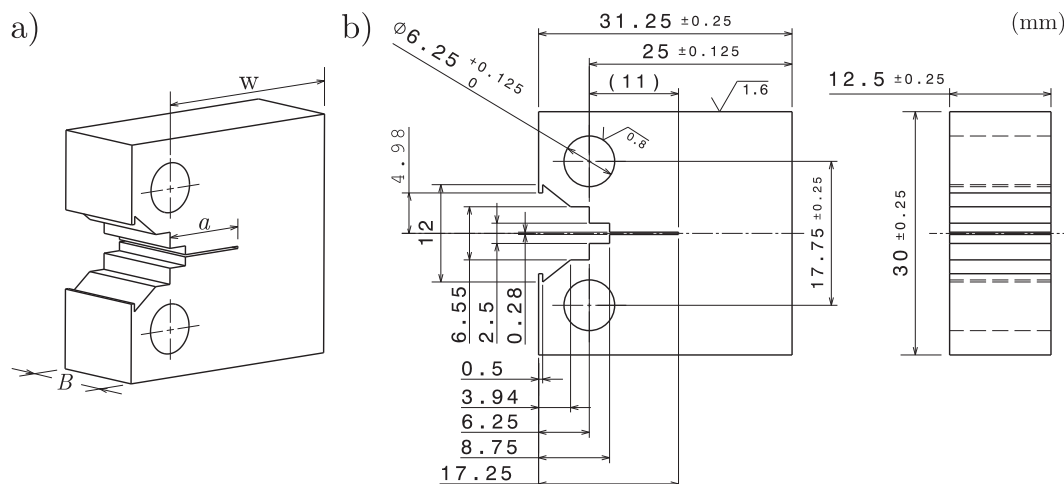


Fig. 1. The geometry of the compact tension specimen used for isothermal fatigue crack propagation (a) isoparametric view showing the variables W , B , and a ; (b) detailed drawing.

variation in both load and temperature impose conditions more representative for the actual investigated component compared to isothermal testing. An OP type of TMF cycle was selected, as it is relevant for the target component, i.e. the inner part of the steam turbine casing. A schematic view of a single OP-TMF cycle is shown in Fig. 2, where the maximum load occurs at the minimum temperature and vice versa. In the present work, both stress controlled and strain controlled tests were performed. For the strain controlled tests, the nominal mechanical strain component, ϵ_{mec} , was controlled, defined as

$$\epsilon_{mec} = \epsilon_{tot} - \epsilon_{th} \quad (3)$$

where ϵ_{tot} is the strain measured by the extensometer, and ϵ_{th} is the thermal strain due to thermal expansion. For both stress and strain control, loading is defined as causing the crack to open and unloading as causing the crack to close (see Fig. 2).

Overall seven specimens were tested in OP-TMF conditions, presented in Table 1, with the same minimum and maximum temperatures, $T_{min} = 100^\circ\text{C}$ and $T_{max} = 600^\circ\text{C}$ respectively. One specimen was tested in stress control with a stress ratio of $R_\sigma = \sigma_{min}/\sigma_{max} = 0$; σ_{min} and σ_{max} being the minimum and maximum nominal stresses during the cycle. The rest of the specimens were tested in strain control with three different mechanical strain ranges, $\Delta\epsilon_{mec}$, of 0.5%, 0.6% and 0.7%, and a strain ratio of $R_\epsilon = \epsilon_{min}/\epsilon_{max} = -\infty$; ϵ_{min} and ϵ_{max} being the minimum and maximum mechanical strains during the cycle. All the specimens were pre-cracked at room temperature prior to the testing with the exception of specimen SET-06 which was cycled twice prior to the pre-cracking under OP-TMF conditions. This is done to support the modelling assumption of the sharp crack not affecting the initial compressive inelastic half cycle.

Single edge crack tension (SET) specimens, displayed in Fig. 3, were used for the TMF testing. The specimens included a manufactured crack starter, shown in the schematic view of detail B in Fig. 3, which acted as an initiation position during pre-cracking to establish a sharp crack. The crack starter was made by EDM and had a nominal length of $l = 2$ mm, while the pre-cracking added 1–2 mm of sharp crack. The actual length of the crack starter, l , for each specimen was measured after machining and presented in Table 1. The combined length of the sharp crack and the crack starter, relative to the outer edge, is referred to as the crack length, a (see Fig. 3). The gauge cross section, see section cut A-A in Fig. 3, was not completely rectangular due to the curved edges, this results in a cross section area of $A_{cs} = 35.62 \text{ mm}^2$. All the specimens were manufactured with turning and the gauge section was produced using EDM. The specimens were manufactured without the application of any additional surface finishing processes.

The cooling and heating rates were the same for all tests and was 5°C/s , giving a cycle length of 200 s/cycle. Some tests were interrupted, then restarted, as indicated in Table 1. The restarting procedure required

compensating for the permanent inelastic strain the specimen had endured. For SET-01, the interruptions were deliberate and made to increase the stress range, $\Delta\sigma$, and the restarts were successful. However, for the SET-02 specimen, an unintended interruption occurred and the restarting was not completely successful which led to an altered strain ratio of approximately $R_\epsilon = -11$, which was different to what was intended (i.e. $R_\epsilon = -\infty$).

An instron 8801 servo hydraulic test machine, shown in Fig. 4, was employed to carry out all the TMF crack propagation tests including thermal profiling, elastic modulus measurement, and pre-cracking. The test machine was equipped with an induction coil surrounding the test specimen as a heating source, while compressed air was used to cool the specimen through three nozzles distributed around the specimen. To ensure proper temperature distribution within the specimen, a thermal profiling procedure was performed at the start of the testing series. This procedure involved attaching a total of six different N-type thermocouples, three on each side of the specimen gauge spaced evenly along the axial direction. The heating from the coil and the air flow from the nozzles were calibrated to obtain a uniform temperature distribution of less than 10°C difference throughout the temperature cycle, as advised by Ref. [24,25]. During testing, the temperature of the specimen was monitored using an N-type thermocouple that was spot-welded at the gauge section. Furthermore, an Instron extensometer 2632-055 with 12.5 mm gauge length was positioned over the crack starter to measure the total strain, ϵ_{tot} . All performed experiments were controlled using Instron TMF software that also carried out a pre-test procedure at the beginning of each test which included thermal stabilisation, thermal strain measurement and validation. The software also contained an elastic modulus measurement procedure that was conducted before pre-cracking to obtain the uncracked stiffness, E_{uncrk} , for each uncracked specimen at 6 different temperatures within the range $100\text{--}600^\circ\text{C}$. In this work, an SET specimen that has a crack starter of length, l , but no sharp crack is defined as uncracked specimen. The elastic modulus measurement was done using an isothermal stress controlled cycle within the elastic limit, i.e. $\pm 20 \text{ MPa}$. For the pre-cracking, the specimens were cycled at room temperature with a stress range of 180 MPa and a stress ratio of $R_\sigma = -1$ at a frequency of 20 Hz.

3. Evaluation methods for thermomechanical fatigue crack propagation

The data obtained from the OP-TMF tests were processed to determine the crack lengths and the stresses at which the crack opens and closes. This was evaluated using a compliance based method [12,26]. The mode I stress intensity factor, K , was calculated with the aid of FE modelling for the SET specimen. Different K values were obtained for the maximum, minimum, opening, and closing nominal stresses, σ_{max} , σ_{min} , σ_{op} and σ_{cl} , respectively, in each cycle giving K_{max} , K_{min} , K_{op} and K_{cl} , respectively. Only mode I K was investigated since the observed crack surface was confirmed to be fairly planar for all tests. The nominal stress, σ_{nom} , during the cycle was defined as

$$\sigma_{nom} = \frac{F}{A_{cs}} \quad (4)$$

where F is the applied force and A_{cs} is the gauge cross section area of the SET specimen with no sharp crack and no crack starter, see section cut A-A in Fig. 3.

3.1. Crack length measurement method

To determine the crack length for the TMF crack propagation tests, a compliance based method adapted for varying temperature was used [12,26,27]. The method utilises the concept that during a test, the change in the crack length, a , produces a change in the normalised stiffness, E_{norm} , of the specimen. By obtaining a function, g , that describes

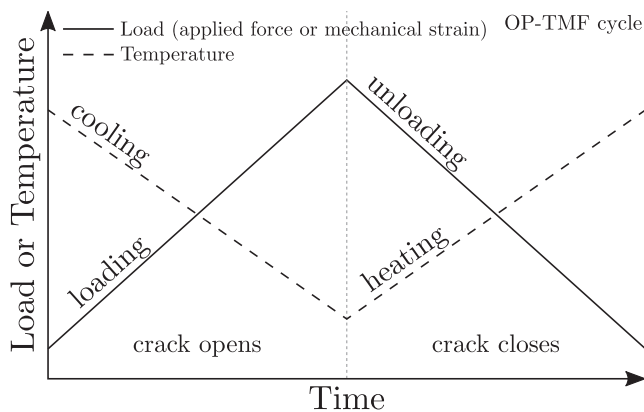


Fig. 2. Schematic illustration of a single out-of-phase thermomechanical fatigue, OP-TMF, crack propagation cycle.

Table 1
Out-of-phase thermomechanical fatigue crack propagation tests performed in this work.

Specimen	T_{\min} , °C	T_{\max} , °C	control	R_e	R_e	$\Delta\sigma$, MPa	$\Delta\epsilon_{\text{mec}}$, %	l , mm	status
SET-01	100	600	Stress	0		200		2.13	Interrupted and restarted
	100	600	Stress	0		250			Interrupted and restarted
	100	600	Stress	0		300			Stopped
SET-02	100	600	Strain		$-\infty$		0.5	2.12	Interrupted and restarted
	100	600	Strain		≈ -11		0.5		Stopped
SET-03	100	600	Strain		$-\infty$		0.5	2.22	Stopped
SET-04	100	600	Strain		$-\infty$		0.6	2.20	Stopped
SET-05	100	600	Strain		$-\infty$		0.6	2.14	Stopped
SET-06	100	600	Strain		$-\infty$		0.6	2.04	Stopped
SET-07	100	600	Strain		$-\infty$		0.7	2.21	Stopped

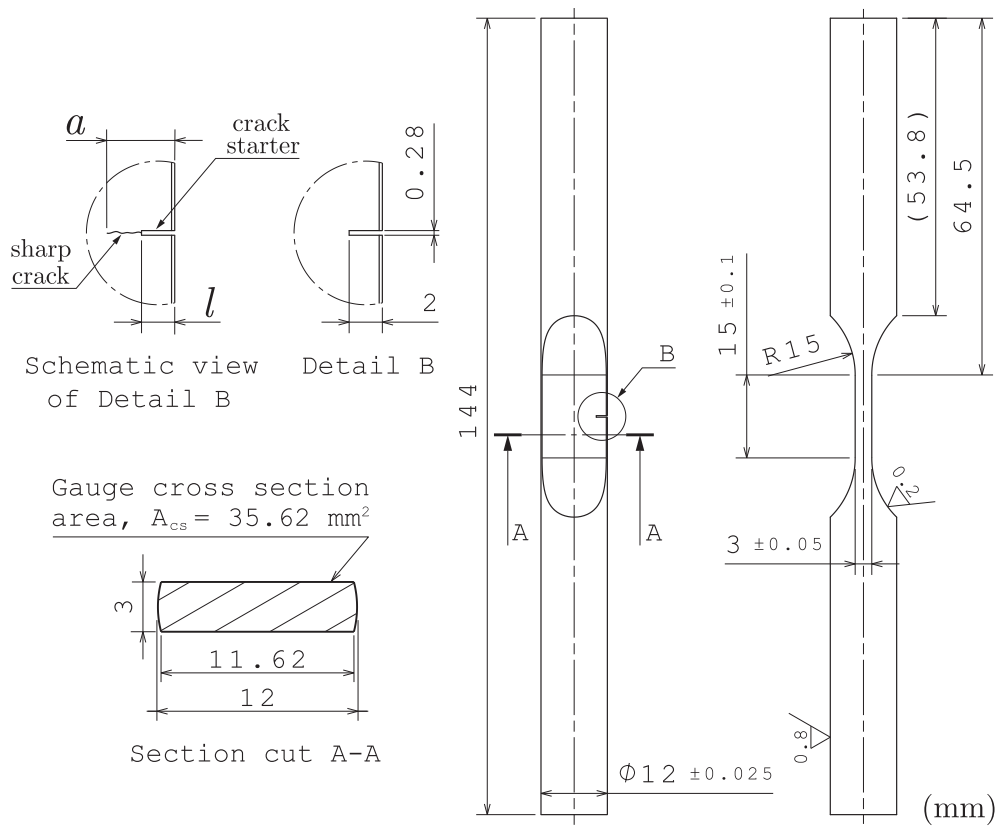


Fig. 3. Detailed drawing of the single edge crack tension specimen used for thermomechanical fatigue crack growth. The schematic view of detail B show the crack length, a , and the crack starter length, l . Section cut A-A shows the gauge cross section area, A_{cs} , with no sharp crack and no crack starter.

the relation between E_{norm} and a , through an FE model, the experimental crack length can be evaluated as

$$a = g(E_{\text{norm}}) \quad (5)$$

where E_{norm} is the normalised stiffness defined as

$$E_{\text{norm}} = \frac{E_{\text{crk}}}{E_{\text{ref}}} \quad (6)$$

where E_{crk} and E_{ref} are the cracked stiffness and the reference stiffness, respectively. During testing, as the crack length, a , increases, E_{crk} drops. For each cycle, the experimental $\sigma_{\text{nom}} - \epsilon_{\text{mec}}$ curve was used to determine E_{crk} from the slope of a line fitted within an elastic unloading interval, see Fig. 5 (a). The interval of elastic unloading must represent a fully open crack as recommended by Ref. [28]. For an OP-TMF cycle, this interval corresponds to the heating of the specimen (see Fig. 2 and Fig. 5 (a)). In this work, the interval was set between $T_1 = 125^\circ\text{C}$ and $T_2 =$

225°C , i.e. starting from T_{\min} plus 5% of ΔT to T_{\min} plus 25% of ΔT , where $\Delta T = T_{\max} - T_{\min}$. The reference stiffness, E_{ref} , is generally computed from the uncracked stiffness. Since existing methods [12,26,27] do not provide a unique definition for E_{ref} , the current work propose

$$E_{\text{ref}} = \frac{\sigma_{\text{nom}}(T_1) - \sigma_{\text{nom}}(T_2)}{\frac{\sigma_{\text{nom}}(T_1)}{E_{\text{uncrk}}(T_1)} - \frac{\sigma_{\text{nom}}(T_2)}{E_{\text{uncrk}}(T_2)}} \quad (7)$$

where σ_{nom} and E_{uncrk} are the nominal stress and the uncracked stiffness, respectively, at temperatures T_1 and T_2 , see Fig. 5. In strain controlled tests, σ_{nom} at T_1 and T_2 can change for each cycle. Fig. 5 (b) shows an example of E_{uncrk} versus temperature obtained from the elastic modulus measurement procedure (discussed at end of Section 2.3) done on the uncracked specimen, SET-05. An uncracked specimen does not have a sharp crack but has a crack starter with a known length, l (see Fig. 3). Since different l was seen for each tested specimen (see Table 1), a

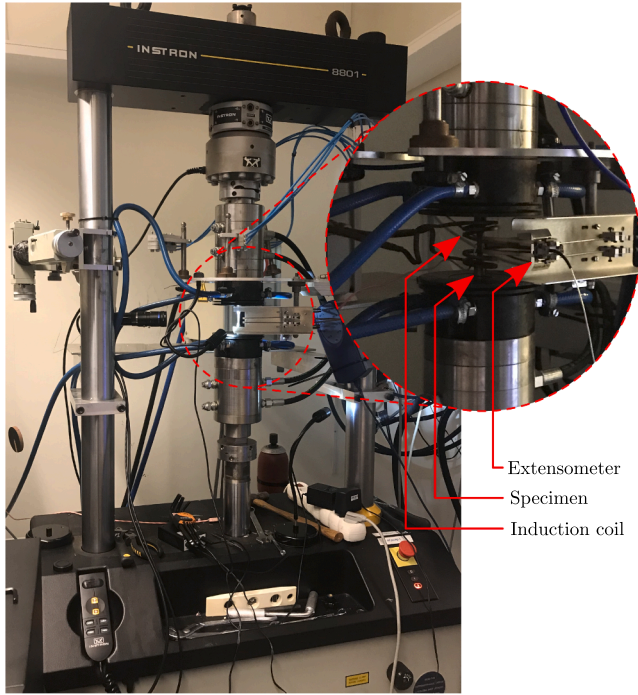


Fig. 4. Instron 8801 servo hydraulic test machine rig used for the thermo-mechanical fatigue crack propagation tests.

unique polynomial function of E_{uncrk} was found for each specimen.

To obtain the function g , a linear elastic FE model of the SET specimen (see Fig. 3) excluding the crack starter was evaluated using the FE software, ABAQUS [29]. The displacement boundary conditions, extensometer sensors locations, and reference nodes were specified as discussed in Section 5.1. The loading was applied in the axial direction on the grips cross section surfaces through the reference nodes (see Section 5.1). The model used an arbitrary elastic modulus of 200 GPa with a stress controlled cycle of $R_\sigma = 0$ and a stress range of 10 kPa. A through-thickness sharp planar crack was inserted between the extensometer sensors with length a_{FE} measured from the outer curvature (same as the definition of crack length, a , in the schematic view of detail B in Fig. 3). Multiple models with different FE crack lengths, a_{FE} , were

created. For each a_{FE} , the FE model stiffness, E_{FE} , was determined from the slope of the modelled $\sigma_{\text{nom}} - \varepsilon_{\text{mec}}$ curve, as shown in Fig. 6. The insertion of different sharp cracks and the remeshing processes were done using Franc3D software [30]. The FE normalised stiffness as a function of the FE crack length, $E_{\text{norm}}^{\text{FE}}(a_{\text{FE}})$, was defined as

$$E_{\text{norm}}^{\text{FE}}(a_{\text{FE}}) = \frac{E_{\text{FE}}(a_{\text{FE}})}{E_{\text{FE}}(l)} \quad (8)$$

where $E_{\text{FE}}(a_{\text{FE}})$ is the FE model stiffness as a function of the FE crack length (see Fig. 6) and $E_{\text{FE}}(l)$ is the FE model stiffness at FE crack length equal to the crack starter length, l . The function g was established by interpolating $E_{\text{norm}}^{\text{FE}}$ as a function of a_{FE} using shape preserving piecewise cubic polynomial [31]. Since the tested specimens had a varying crack starter length, l , (see Table 1) a unique function g was produced for each SET specimen.

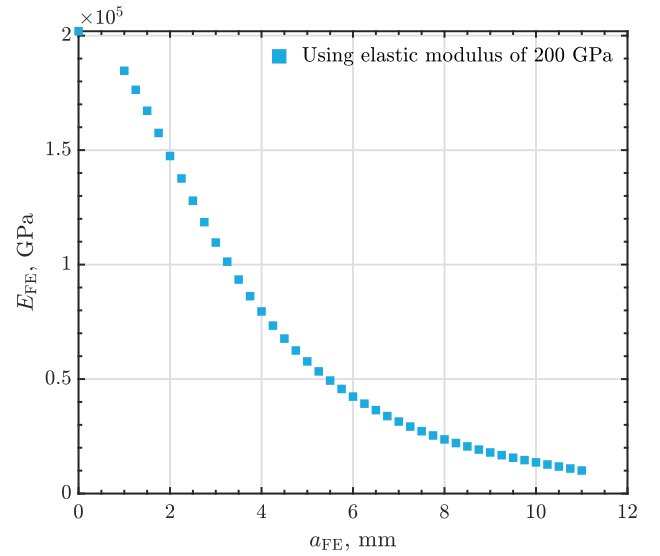


Fig. 6. The FE model stiffness, E_{FE} , as a function of the FE crack length, a_{FE} , produced from the linear elastic FE model of the SET specimen excluding the crack starter.

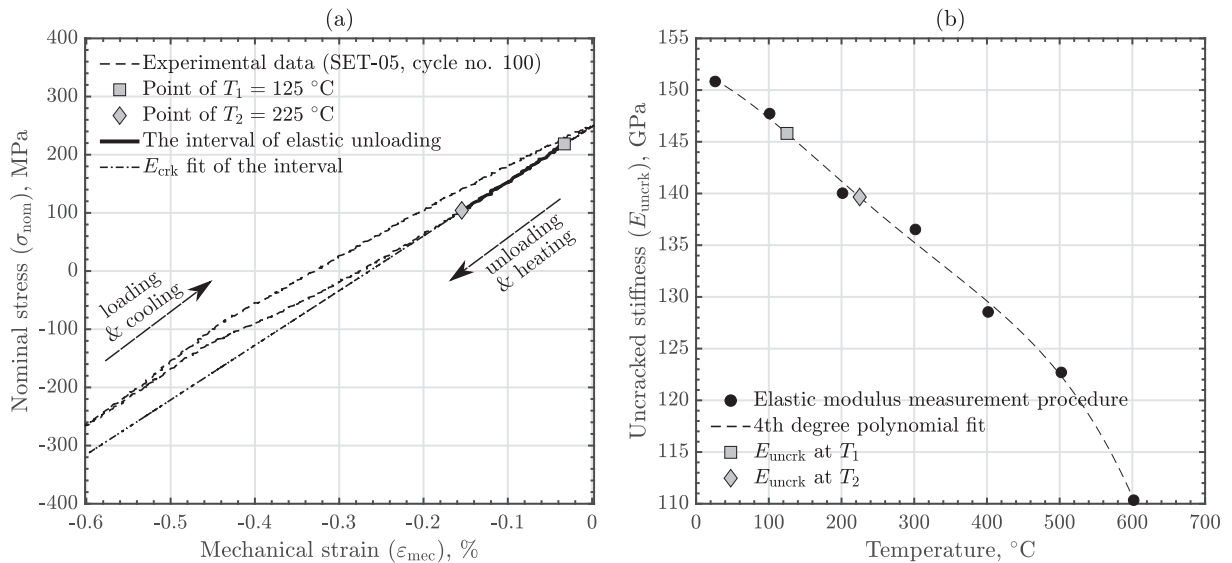


Fig. 5. An example describes the crack length measurement method applied on specimen SET-05, showing (a) the experimental $\sigma_{\text{nom}} - \varepsilon_{\text{mec}}$ curve at cycle 100; (b) the uncracked stiffness, E_{uncrk} , as a function of temperature.

3.2. Crack closure stress measurement method

The presence of a macrocrack within the specimen would produce a noticeable change in its stiffness depending on whether the crack faces are being in contact or not. Following this concept, a compliance based method to assess crack closure while accounting for the variation in temperature, due to TMF conditions, was developed by [12]. The method determines crack closure by defining a degree of crack opening, D_{op} , that goes from 0, crack being fully closed, to 1, crack being fully open, as the load increases during the loading of the TMF cycle. By defining a limit for D_{op} that corresponds to the crack being open, i.e. close to 1, the opening nominal stress, σ_{op} can be determined. In the current work, a degree of crack closing, D_{cl} , is introduced, which is applied during the unloading of the TMF cycle (see Fig. 2). Thus, D_{cl} goes from 1 to 0 instead, producing the closing nominal stress, σ_{cl} , when it is close to 1, i.e. the crack just begins to close but still completely open. The definition proposed by [12] for D_{op} was modified to include E_{ref} , introduced in Eq. (7), as

$$D_{op} = \frac{1 - \frac{E_{ld}}{E_{ref}}}{1 - E_{norm}} \quad (9)$$

and for D_{cl} as

$$D_{cl} = \frac{1 - \frac{E_{unld}}{E_{ref}}}{1 - E_{norm}} \quad (10)$$

where E_{ld} and E_{unld} are the tangent stiffnesses during the loading curve and the unloading curve, respectively. For each curve, i.e. loading or unloading, the tangent stiffness, i.e. E_{ld} or E_{unld} , evaluation was done at sixty different stress points equally spaced along the nominal stress range of the cycle, see Fig. 7 (a). Each stress point has an overlapping interval of 5% of the nominal stress range in the cycle. As shown in Fig. 7 (a), the tangent stiffness was obtained from the slope of a line fitted within the stress point interval, where E_{ld} was from points on the loading curve and E_{unld} was from points on the unloading curve. The minimum and maximum temperatures within each stress point interval were set to T_1 and T_2 , respectively, to compute E_{ref} by Eq. (7). Furthermore, E_{norm} was obtained for each cycle from Eq. (6) as described in Section 3.1. Thus, unique E_{ld} and E_{ref} values were obtained for each stress point on the loading curve, producing D_{op} versus nominal stress, σ_{nom} , for each cycle. Also, unique E_{unld} and E_{ref} values on the unloading curve, producing D_{cl} versus σ_{nom} for each cycle. Fig. 7 (b) shows the evolution of

D_{op} and D_{cl} over a single cycle for SET-05 test (OP-TMF $\Delta\epsilon_{mec} = 0.6\%$) at cycle 100.

The choice of suitable levels for D_{op} and D_{cl} to obtain σ_{op} and σ_{cl} is necessary to produce reliable crack closure results. [12] found that using $D_{op} = 0.9$ would produce a 6% overestimation of the effective stress intensity range. However, $D_{op} = 0.9$ was considered usable since higher values of D_{op} would increase the scatter and complicate the evaluation of short crack lengths. Consequently, D_{op} and D_{cl} equal to 0.9 were used to produce σ_{op} and σ_{cl} for all tests in this work (an example is shown in Fig. 7 (b)).

3.3. Crack growth assessment method

The crack growth assessment method for the TMF tests is based on LEFM and utilises the stress intensity factor. This is justified since the hysteresis loops were close to linear elastic. The majority of the inelastic deformation occurred during the first few cycles of the TMF test (as will be shown later). For the SET specimen, the mode-I stress intensity factor, K , takes the general form

$$K = \sigma_{nom} \sqrt{\pi a} f_{SET} \left(\frac{a}{W} \right) \quad (11)$$

where f_{SET} is the geometrical factor for the SET specimen with a width $W = 12$ mm (see Fig. 3). To obtain f_{SET} , the linear elastic FE model introduced in Section 3.1 was used. For each a_{FE} , an average mode I FE stress intensity factor, K_{FE} , was computed along the crack front (excluding one value from the end of each side) through the built-in routines in Franc3D [30]. The software utilises a path-independent line integral around the crack tip to compute the stress intensity factor. The geometrical factor, f_{SET} , was evaluated at several normalised crack length, a/W , as shown in Fig. 8, and fitted using a 7th degree polynomial function,

$$f_{SET} \left(\frac{a}{W} \right) = 261.22 \left(\frac{a}{W} \right)^7 - 772.7 \left(\frac{a}{W} \right)^6 + 918.2 \left(\frac{a}{W} \right)^5 - 556.4 \left(\frac{a}{W} \right)^4 + 180.51 \left(\frac{a}{W} \right)^3 - 28.49 \left(\frac{a}{W} \right)^2 + 2.692 \left(\frac{a}{W} \right) + 1.12. \quad (12)$$

The geometrical factor, f_{SET} , is then used in Eq. (11) to compute K for any nominal stress, σ_{nom} , in the experimental cycle for which the crack length, a , is known.

The fatigue crack growth was characterised by Paris law [32]

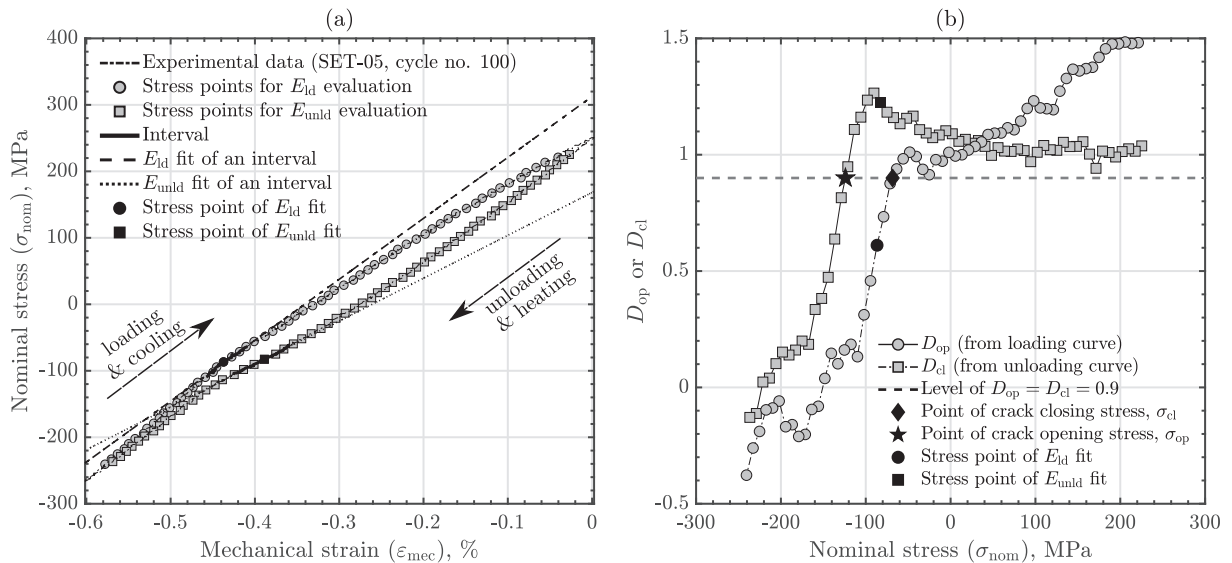


Fig. 7. An example describes the crack closure measurement method applied on specimen SET-05 at cycle 100, showing (a) the experimental $\sigma_{nom} - \epsilon_{mec}$ curve; (b) the degree of crack opening and closing, D_{op} and D_{cl} , as a function of the nominal stress, σ_{nom} .

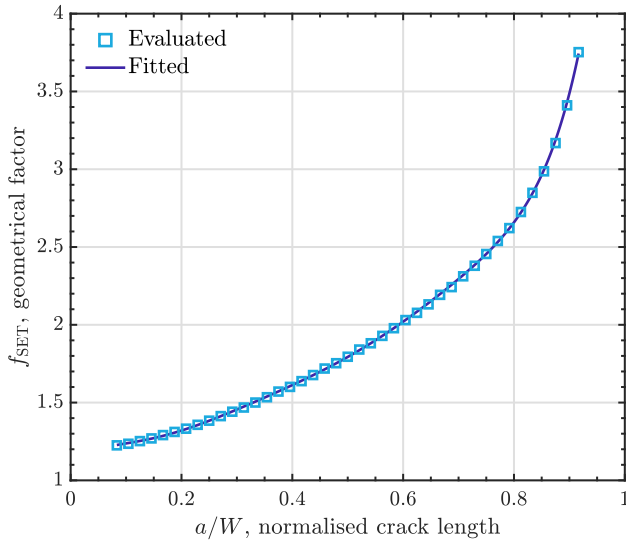


Fig. 8. The geometrical factor for the SET specimen, f_{SET} , as a function of normalized crack length, a/W .

$$\frac{da}{dN} = \tilde{C} \Delta K^{\tilde{m}} \quad (13)$$

where the relation between the crack growth rate, da/dN , and the stress intensity range, ΔK , follows a power law relationship with \tilde{C} and \tilde{m} being material parameters. Various definitions of ΔK exist [28], most common is to exclude the compressive part of the cycle, i.e. negative stress intensities, giving

$$\Delta K = \begin{cases} K_{\max} - K_{\min} & \text{if } K_{\min} > 0 \\ K_{\max} & \text{if } K_{\min} \leq 0 \\ 0 & \text{if } K_{\max} \leq 0 \end{cases} \quad (14)$$

where K_{\max} and K_{\min} correspond to the stress intensity factor at σ_{\max} and σ_{\min} , respectively. An alternative definition is using the full stress range giving the full range stress intensity factor, ΔK_{fr} , as

$$\Delta K_{fr} = K_{\max} - K_{\min}. \quad (15)$$

To account for crack closure effects that influence the crack growth

behaviour, only the part of the cycle that correspond to the crack being fully open is considered [8]. For the loading part of the cycle

$$\Delta K_{eff,op} = K_{\max} - K_{op} \quad (16)$$

where $\Delta K_{eff,op}$ and K_{op} are the effective opening stress intensity range and the stress intensity factor at σ_{op} , respectively. For the unloading part of the cycle

$$\Delta K_{eff,cl} = K_{\max} - K_{cl} \quad (17)$$

where $\Delta K_{eff,cl}$ and K_{cl} are the effective closing stress intensity range and the stress intensity factor at σ_{cl} , respectively.

4. Experimental results

All strain controlled OP-TMF crack propagation tests were done in negative mechanical strain (except for the restarted test of SET-02 with a slight positive ϵ_{mec} of about 0.04 %). The main driving factor for crack growth came from tensile stresses introduced as a result of the first half-cycle being inelastic. Fig. 9 (a) shows $\sigma_{nom} - \epsilon_{mec}$ curves for test SET-05 (OP-TMF $\Delta \epsilon_{mec} = 0.6\%$) with excessive plasticity and creep in the first half-cycle, especially above 500 °C, causing tensile stress as ϵ_{mec} returned to zero. For all strain controlled tests, σ_{\min} of the first cycle reached a similar level between -294 MPa to -350 MPa, followed by relaxation with cycles suggesting that creep is the main controlling factor of σ_{\min} after the initial plasticity during the first half-cycle. On the other hand, for σ_{\max} , a dependency on a , $\Delta \epsilon_{mec}$, and R_e , was observed for the strain controlled OP-TMF tests.

The isothermal crack propagation test at 100 °C and the stress controlled OP-TMF test, SET-01, (at all stress ranges) showed no signs of crack closure as no change in the stiffness was observed in the $\sigma_{nom} - \epsilon_{mec}$ curves. However, all the strain controlled OP-TMF crack propagation tests showed visible changes in the stiffness below zero nominal stress for all cycles, suggesting premature crack opening and closing, e.g. see Fig. 9 (a). To account for this effect, the nominal stresses at which the crack closure occurred during the loading and the unloading parts of the cycle, σ_{op} and σ_{cl} respectively, were calculated for all strain controlled tests using the method discussed in Section 3.2. Fig. 9 (b) shows an example of crack opening and closing stresses, σ_{op} and σ_{cl} , for SET-05 (OP-TMF $\Delta \epsilon_{mec} = 0.6\%$). The σ_{op} and σ_{cl} were not necessary equal and the largest difference between them occurred at short crack lengths. However, the difference reduces as the crack length increases with

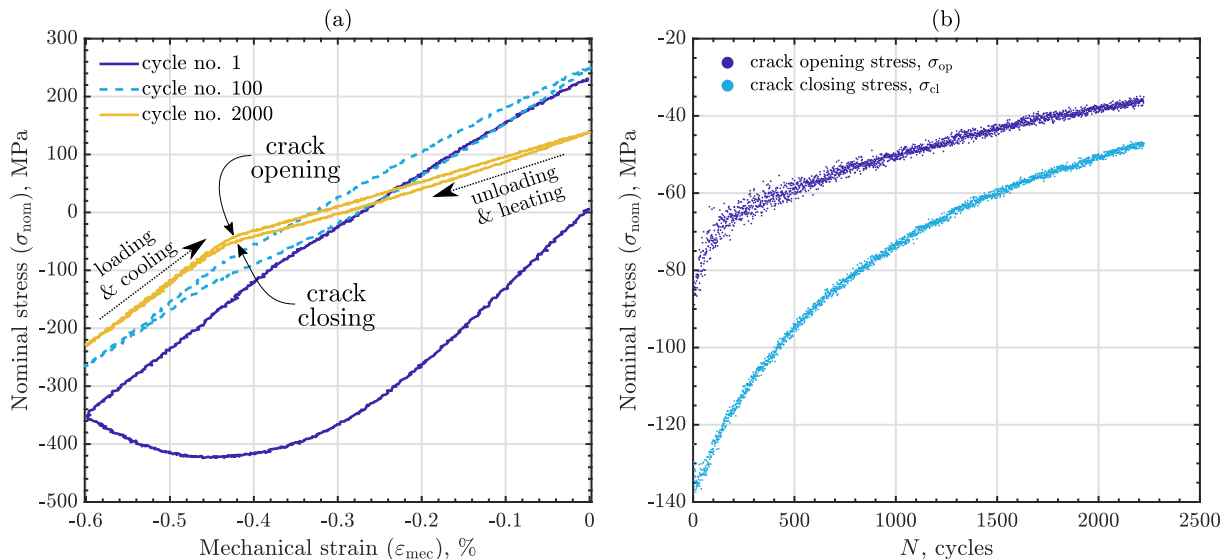


Fig. 9. The SET-05 specimen tested under 100–600 °C OP-TMF, $\Delta \epsilon_{mec} = 0.6\%$ showing (a) experimental $\sigma_{nom} - \epsilon_{mec}$ curves at cycles 1, 100 and 2000; (b) crack opening and closing stresses, σ_{op} and σ_{cl} , as a function of cycles, N .

cycles, see Fig. 9 (b).

Fig. 10 (a) shows the crack growth rate, da/dN , versus ΔK , i.e. the stress intensity range for the tensile part of the cycle. All strain controlled OP-TMF tests appear to give faster crack growth rates than both stress controlled OP-TMF (SET-01) and isothermal crack growth at 100 °C. Also, lower $\Delta\epsilon_{mec}$ gives faster crack growth than large $\Delta\epsilon_{mec}$. However, for the restarted SET-02 test (OP-TME $\Delta\epsilon_{mec} = 0.5\%$), the increase in R_e , from $-\infty$ to -11 , gave lower crack growth rates, as shown in Fig. 10 (a). On the other hand, using the full stress intensity range, ΔK_{fr} , presented in Fig. 10 (b), showed no improvement in the prediction of the crack growth behaviour.

By accounting for crack closure, as shown in Fig. 11, the crack growth rates for the different tests tend to collapse on a single master curve. In Fig. 11 (a), $\Delta K_{eff,op}$ was used to account for closure captured from the loading part of the experimental cycle (see Eq. (16)), while in Fig. 11 (b), $\Delta K_{eff,cl}$ was used to account for closure captured from the unloading part of the experimental cycle (see Eq. (17)).

For all strain controlled tests, the crack growth rate starts from the highest value and decreases with cycles, unlike stress control tests where crack growth rate starts from the lowest value and increases with cycle, see Figs. 10 and 11. It can be observed that the initial part of the tests done at $\Delta\epsilon_{mec} = 0.5\%$ OP-TMF (SET-02 and SET-03) shows a large decrease in crack growth rate at constant stress intensity range. However, this was not observed for the other strain ranges. The shift in R_e , due to test interruption, for SET-02 (OP-TMF $\Delta\epsilon_{mec} = 0.5\%$) shifted the crack growth rate to a slightly different level (see Fig. 10); however, when accounting for crack closure, the growth behaviour followed the main trend (see Fig. 11).

5. Finite element modelling of crack closure

To predict the crack closure behaviour seen in the strain controlled OP-TMF tests, a three dimensional finite element model of the SET specimen with a stationary sharp crack was set up. Three different strain controlled OP-TMF tests with $\Delta\epsilon_{mec}$ of 0.5 %, 0.6 %, and 0.7 %, all with $R_e = -\infty$, were simulated. Each model was simulated with 7 different crack lengths, a , of 3.15 mm, 3.5 mm, 4.0 mm, 4.5 mm, 5.0 mm, 5.5 mm, 6.0 mm. The stress controlled OP-TMF test was also simulated to confirm

the non-existence of crack closure behaviour using the FE model.

5.1. Boundary conditions, loading, and mesh

Full SET specimen (see Fig. 3) with a crack starter of exactly 2 mm was modelled using the FE software ABAQUS [29]. Boundary conditions and loading were applied as shown in Fig. 12 to generate an FE model close the actual crack propagation test. The ends of the specimen were sectioned at the centre, perpendicular to the X and Z directions, to apply displacement constraints that fixes the specimen in the X and Z directions, see Fig. 12 a). Moreover, the displacement in the Y direction was fixed at the middle and through the thickness of the gauge section. At each end of the specimen, all nodes on the grip's cross section surface were coupled, using kinematic coupling, to a reference node, as shown in Fig. 12 b). In kinematic coupling, all nodes on the surface follow the same movement as the reference node connected to it.

The mechanical loading was applied uniaxially on the specimen as force in the Y-direction through the reference nodes (see Fig. 12 a)). The desired mechanical strain, ϵ_{mec} , was obtained using two sensors, located at the same location as the actual extensometer rods. Since no thermal expansion was included in the model, the total strain computed from the sensors was equivalent to the mechanical strain. Furthermore, to achieve OP-TMF conditions, a time dependent uniform temperature field was assigned to the whole specimen. Strain controlled testing was simulated using user defined amplitude subroutine where the applied load on the reference nodes was controlled to achieve the desired ϵ_{mec} from the sensors. The modelled SET specimen was meshed, as shown in Fig. 13, using quadratic hexahedron elements with reduced integration. Fig. 13 b) shows the mesh refinement within the gauge section.

5.2. Sharp crack and contacts conditions

A sharp planar crack was inserted at the root of the crack starter, see Fig. 12 a). This was done by defining a through thickness surface and duplicating all nodes on it (except for the nodes at the tip) creating two set of nodes on each face of the crack. A contour mesh was used around the crack tip, as shown in Fig. 13 b). The elements at the tip were hexahedron elements collapsed to wedge elements to improve the strain

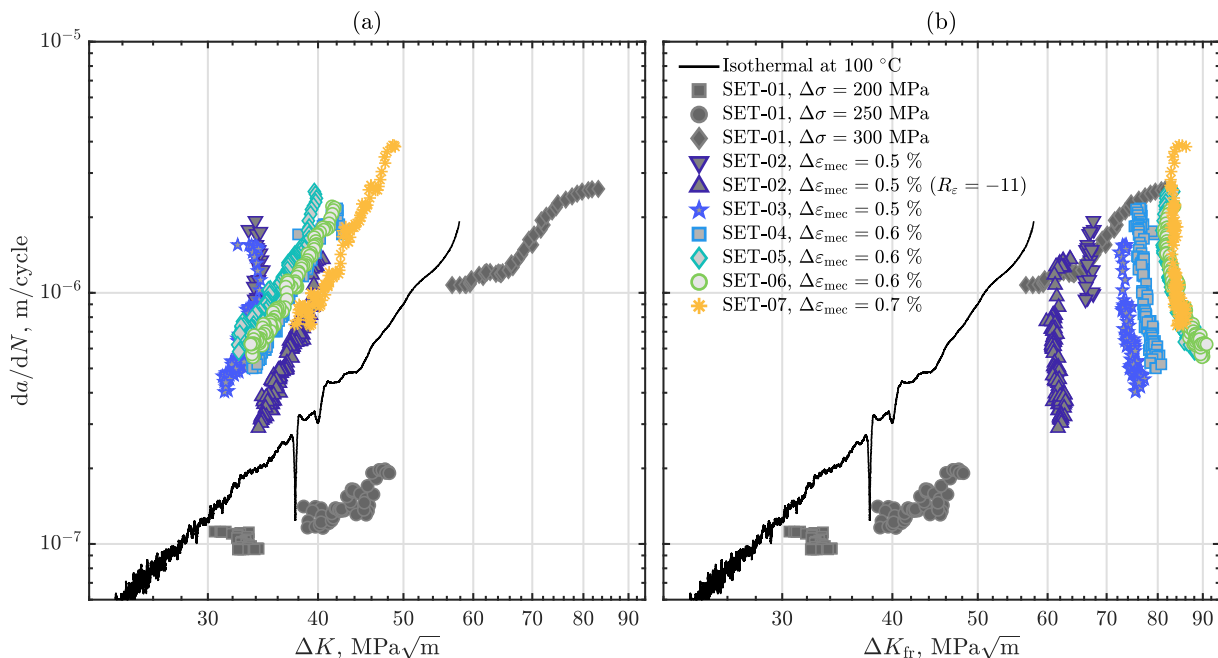


Fig. 10. Fatigue crack growth behaviour without accounting for crack closure, using (a) da/dN versus ΔK (only tensile part of the fatigue cycles); (b) da/dN versus ΔK_{fr} (full range of the fatigue cycles).

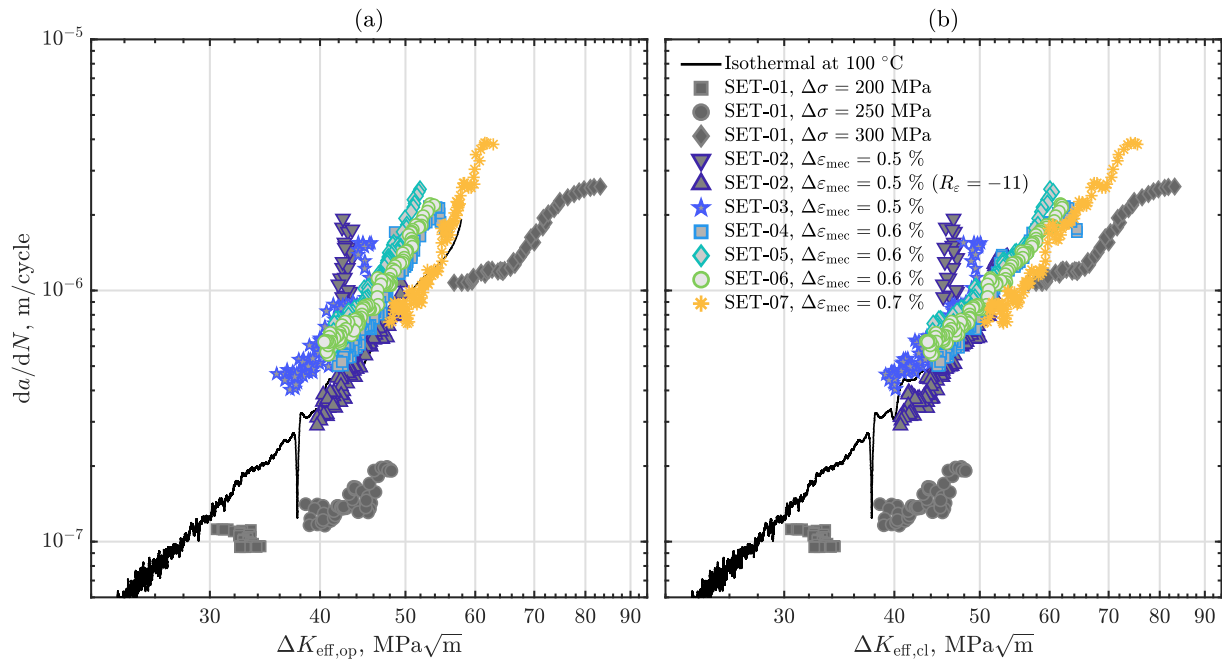


Fig. 11. Fatigue crack growth behaviour accounting for crack closure, using (a) da/dN versus $\Delta K_{eff,op}$ (closure level from the loading part of the cycle); (b) da/dN versus $\Delta K_{eff,cl}$ (closure level from the unloading part of the cycle).

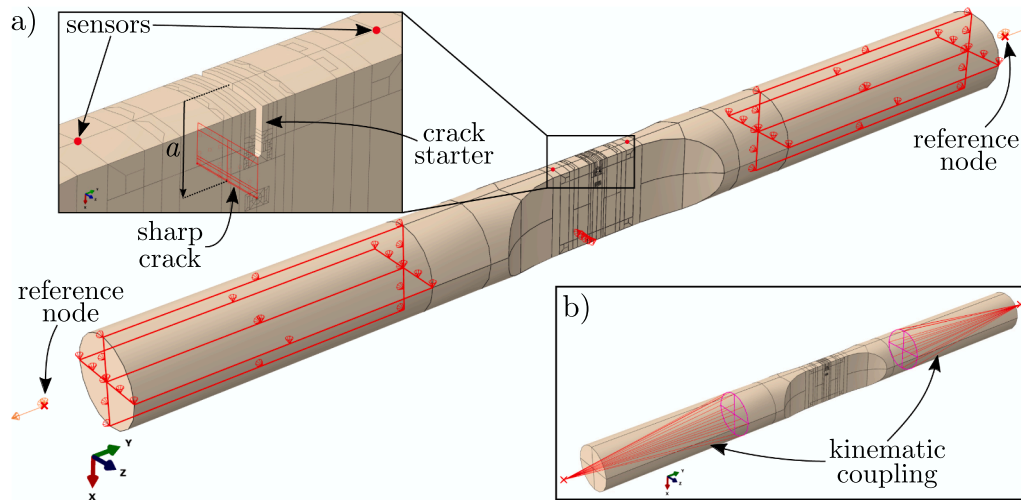


Fig. 12. The FE model of SET specimen used for simulating OP-TMF tests showing, a) boundary conditions, sensors, and reference nodes; b) kinematic coupling between reference nodes and the grip's cross section surfaces.

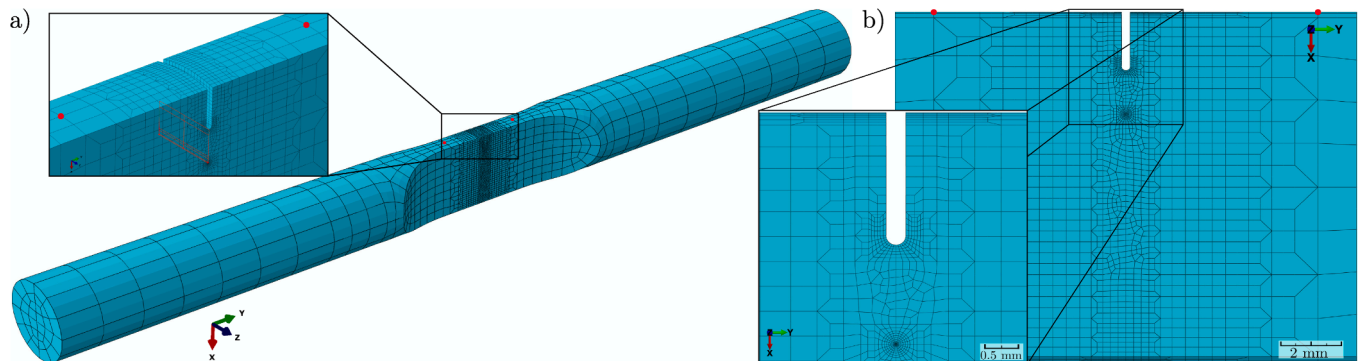


Fig. 13. Meshing of the FE model showing, a) the modelled SET specimen and mesh refinement through the gauge thickness; b) mesh refinement within the gauge section.

singularity. In addition, the nodes that were collapsed at the same geometrical location were constrained to move together as a single node. The crack tip mid-side nodes were moved closer to the tip (30% away from crack tip). This produced a crack tip singularity suitable for linear elastic models [29]. Contact conditions were applied on the sharp crack surface to prevent interpenetration during compressive load. Self-contact condition was used, which can be thought of as a surface that has been completely folded to form the sharp crack. The contact formulation used was a finite-sliding tracking approach with surface-to-surface discretisation. For the mechanical properties of the contacts, rough friction was used, which implies that no slipping occurs once the crack surfaces are in contact. For the contact constraint enforcement, a linear penalty method was used, which implies that transmission of contact pressure occurs only when the surfaces are in contact and the contact force is linearly proportional to the penetration distance.

5.3. Material models

The FE simulations in this work used both cyclic elasto-plastic and creep material models, which were provided by the FE software, ABAQUS [29], as built-in constitutive models. All the parameters employed to calibrate the material models were extracted from separate isothermal low cycle fatigue (LCF) testing on smooth cylindrical specimens done in a previous work by the authors, see [17]. These tests were done on the same steel, FB2, and from the same material batch. The parameters for the elasto-plastic model were extracted from the monotonic loading of the first half-cycle and the parameters for the creep model were taken from LCF cycles with dwell times.

A linear elastic model and a nonlinear kinematic hardening model with two back-stresses were used for the elasto-plastic material model. An associated flow rule with von Mises yield criteria was utilised. The evolution law of the hardening model consisted of Ziegler's kinematic law plus a recall term for each of the back-stresses, α_m , [29]

$$\dot{\alpha}_m = C_m \frac{\sigma - \alpha_m^p}{\sigma_y} \dot{\epsilon}^p - \gamma_m \alpha_m \dot{\epsilon}^p \quad (18)$$

with the total back-stress tensor

$$\alpha = \sum_{m=1}^2 \alpha_m \quad (19)$$

where C_m and γ_m are temperature dependent material parameters with $m = 1, 2$, while $\dot{\alpha}_m$, σ , σ_y , and $\dot{\epsilon}^p$ are the rate of the back-stress tensor, the stress tensor, the yield strength, and the equivalent plastic strain rate, respectively. The temperature dependent material parameters used for the elasto-plastic model are presented in Table 2 where E and ν are the elastic modulus and Poisson's ratio, respectively, while $\Delta\epsilon_{mec}$ is the mechanical strain range of the LCF test at which the kinematic hardening parameters were taken from.

The creep behaviour was modelled using a Norton power law as [33]

$$\dot{\epsilon}^c = A \tilde{\sigma}^n \quad (20)$$

where $\dot{\epsilon}^c$ and $\tilde{\sigma}$ are the equivalent creep strain rate and the equivalent stress, respectively, while A and n are temperature dependent fitted

material parameters.

These parameters were fitted for the first few cycles at the dwell region in tension for the LCF tests with dwell times. The fitting procedure to obtain the creep parameters is explained in details in [17]. The parameter A was fitted using an Arrhenius type equation and n using a 2nd degree polynomial. These fits were used to obtain the creep parameters at any desired temperature. Table 3 presents the fitted creep parameters for each tested temperature. All the temperature dependent material parameters presented in Table 2 and 3 were interpolated over the temperature range 100–600 °C (extrapolated to 100 °C in the case of creep parameters) for every 10 °C prior to including them in the FE model.

5.4. Verification of the finite element model

The first few cycles of the strain controlled OP-TMF tests were simulated to check the accuracy of the FE model. Fig. 14 shows a comparison of $\sigma_{nom} - \epsilon_{mec}$ curves from the experiments and the FE simulation for SET-06 (OP-TMF, $\Delta\epsilon_{mec} = 0.6\%$), which was cycled a few times without a sharp crack (prior to pre-cracking). The FE simulation showed a satisfactory prediction considering that the material model was calibrated using isothermal LCF tests. This also indicates that the applied loading, boundary conditions, and mesh were acceptable.

The strain controlled OP-TMF tests with the first $\sigma_{nom} - \epsilon_{mec}$ cycle done after pre-cracking were simulated by including sharp crack and contact conditions in the FE model (see Section 5.2). The simulated 100–600 °C OP-TMF tests were SET-2 and SET-03 at $\Delta\epsilon_{mec} = 0.5\%$, SET-05 at $\Delta\epsilon_{mec} = 0.6\%$, and SET-07 at $\Delta\epsilon_{mec} = 0.7\%$, as shown in Fig. 15 (a), (b), and (c), respectively. For all the three FE simulations, $a = 3.5$ mm was modelled, since the first cycle of all the experimental tests were observed to have approximately similar crack lengths. The $\sigma_{nom} - \epsilon_{mec}$ curves in Fig. 15 show sufficiently accurate agreement between the experiments and the FE simulations. Thus, the sharp crack and the contact conditions implemented in the FE model are justified. Furthermore, by observing Fig. 14 and Fig. 15 (b), it can be seen that the assumption of including a fully closed sharp crack in the FE model was valid, since similar inelastic behaviour was achieved during the compression part of the first cycle with or without the sharp crack. Although further cycling would relax the minimum stress, σ_{min} , in the experimental result (see Fig. 9 (a)), the FE simulations were not adapted to capture this behaviour and only a small relaxation occurred before a stable σ_{min} was reached (around –300 MPa after 5 simulated cycles) for all simulated $\Delta\epsilon_{mec}$ and crack lengths. It should be noted that the crack starter did not close during compression in either the experimental or the FE results.

Table 3

Temperature dependent material parameters, A and n , for the Norton power law creep model.

Temperature, °C	A , 1/(GPa ⁿ ·s)	n
500	6.65×10^4	30.27
550	8.10×10^2	19.95
600	16.37	13.69

Table 2

The elasto-plastic temperature dependent material parameters used for simulating OP-TMF crack propagation tests.

Temperature, °C	E , GPa	ν	$\Delta\epsilon_{mec}$, %	σ_y , MPa	C_1 , MPa	C_2 , MPa	γ_1	γ_2
20	213.97	0.285	2.0	588.40	44,680	322,985	426.07	4157.7
400	186.69	0.299	1.2	481.22	85,958	229,111	828.84	5821.7
500	179.91	0.305	1.2	420.31	101,264	257,438	870.96	5782.6
550	170.24	0.308						
600	159.41	0.312	1.2	300.20	118,360	584,880	1056.4	7054.7
625	147.36	0.314						

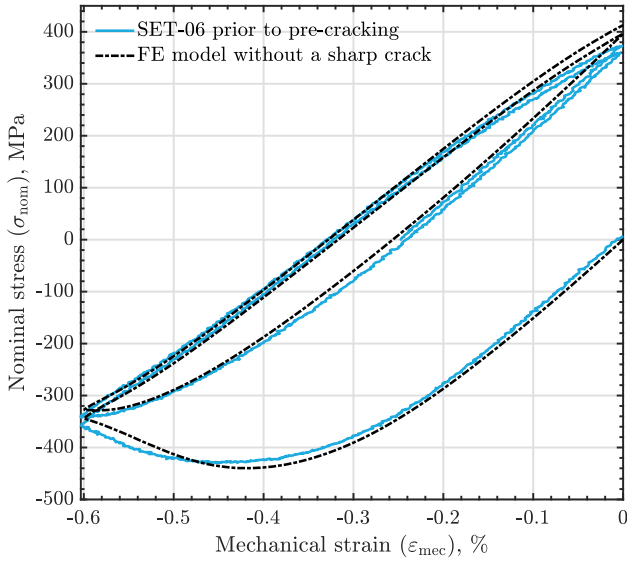


Fig. 14. Experimental and modelled $\sigma_{\text{nom}} - \varepsilon_{\text{mec}}$ curves for SET-06 (OP-TMF, $\Delta\varepsilon = 0.6\%$) cycled prior to pre-cracking (without sharp crack).

5.5. Finite element crack closure prediction

The stationary sharp crack with contact conditions in the FE model caused a change in the stiffness below zero nominal stress, i.e. crack closure. This change in the stiffness could be observed from the loading of the first modelled cycle for all simulated $\Delta\varepsilon_{\text{mec}}$ and crack lengths, e.g. see Fig. 15. To determine the crack closure level in the FE simulations, the crack closure stress measurement method, discussed in Section 3.2, was used. The method was applied on both the loading and the unloading part of the modelled cycle to obtain the FE crack opening stress, σ_{op} , and the FE crack closing stress, σ_{cl} . All the FE simulations were run for 5 cycles so that a stable closure stresses were reached; however, it was observed that the FE σ_{cl} stabilises faster (on the 2nd cycle) than the FE σ_{op} . Nevertheless, σ_{op} and σ_{cl} from all the FE simulations were taken from the 5th modelled cycle. Fig. 16 shows the experimental and FE modelled crack closure stresses (σ_{op} and σ_{cl}) as a function of the crack length, a . The FE crack opening and closing stresses were interpolated over a using a shape preserving piecewise cubic

polynomial [31]. For both experimental and FE results, σ_{op} shows a rather weak dependence on $\Delta\varepsilon_{\text{mec}}$ (see Fig. 16 (a)), while σ_{cl} shows a larger distinction with $\Delta\varepsilon_{\text{mec}}$ (see Fig. 16 (b)). In general, the FE crack closure stresses (σ_{op} and σ_{cl}) seem to predict the experimental results better for short crack lengths. Nevertheless, the maximum difference between the experimental and FE computed crack closure stresses was relatively small, i.e. ≈ 20 MPa. Thus, the FE predictions for the crack closure stresses were acceptable. Furthermore, the FE simulations seem to predict the difference between the opening and closing of the crack, i.e. the difference between σ_{op} and σ_{cl} , see Fig. 16.

The stress intensity factors for FE σ_{op} and FE σ_{cl} , i.e. $FE K_{\text{op}}$ and $FE K_{\text{cl}}$, were computed using Eq. (11). This allowed the computation of the FE effective opening and closing stress intensity ranges, i.e. $FE \Delta K_{\text{eff,op}}$ and $FE \Delta K_{\text{eff,cl}}$, respectively, using Eq. (16) and (17). By accounting for the crack closure effects through the FE simulations, the crack growth curves collapses together using both $FE \Delta K_{\text{eff,op}}$ and $FE \Delta K_{\text{eff,cl}}$, as shown in Fig. 17. However, the crack growth behaviour seem to align better with the OP-TMF stress controlled tests and the isothermal crack propagation test when using the FE effective closing stress intensity range, $FE \Delta K_{\text{eff,op}}$, as seen in Fig. 17 (b).

6. Discussion

The crack closure measurement in the current study was based on the change in the specimen's global stiffness obtained from the $\sigma_{\text{nom}} - \varepsilon_{\text{mec}}$ curves following a compliance method adapted for TMF conditions (see Section 3.2). Local measurement of crack opening stress using two-dimensional FE model with a node-release scheme has been seen to correlate well with the use of compliance method [7]. Both the experimental and the modelled crack closure stresses in the current work (see Fig. 16) were produced by the compliance method for the same threshold level of D_{op} and D_{cl} , i.e. 0.9.

Accounting for crack closure from the experimental $\sigma_{\text{nom}} - \varepsilon_{\text{mec}}$ cycles, as shown in Fig. 11, seem to align all strain controlled tests with the results from the stress control OP-TMF tests (SET-01) and the isothermal fatigue crack propagation test at 100°C (which did not change since no crack closure was detected). This shows that OP-TMF crack growth in the studied material (FB2) is largely determined by the low temperature part of the cycle, i.e. at 100°C . It could also be seen, in Fig. 11, that using $\Delta K_{\text{eff,cl}}$ collapsed the curves for all strain controlled tests better than $\Delta K_{\text{eff,op}}$, especially for large stress intensity range values where the crack

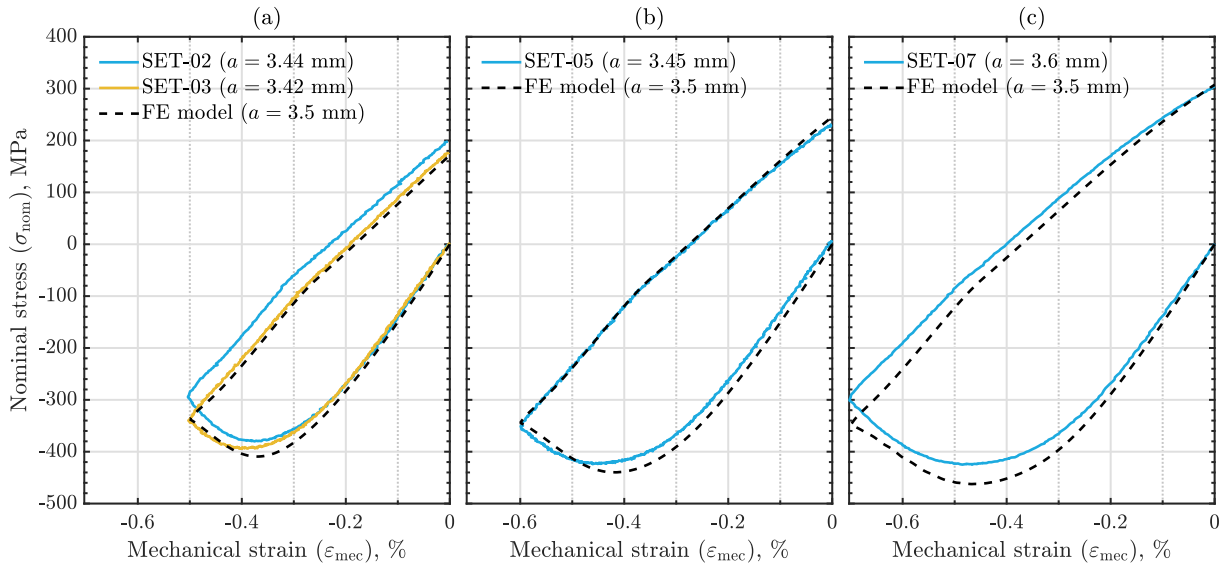


Fig. 15. Experimental and modelled $\sigma_{\text{nom}} - \varepsilon_{\text{mec}}$ curves for the 1st cycle of OP-TMF test with sharp crack and $\Delta\varepsilon_{\text{mec}}$ of (a) 0.5 %, (b) 0.6 %, and (c) 0.7 %; where a is the crack length.

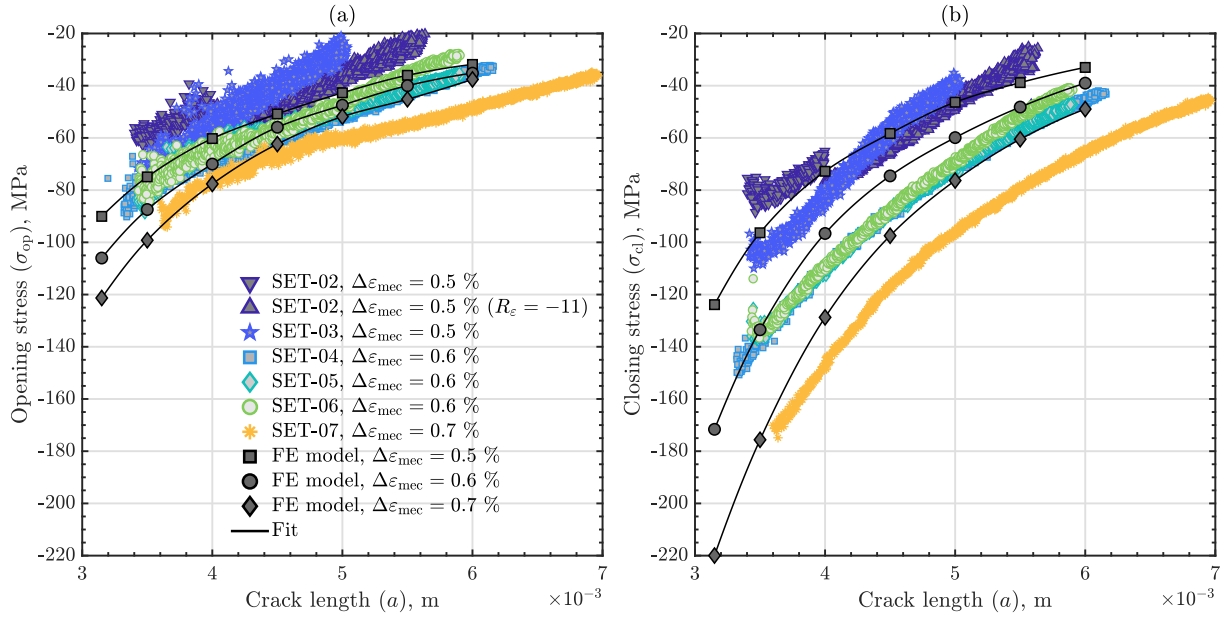


Fig. 16. Experimental and numerical crack closure levels as a function of crack length, a using (a) crack opening stress, σ_{op} ; (b) crack closing stress, σ_{cl} .

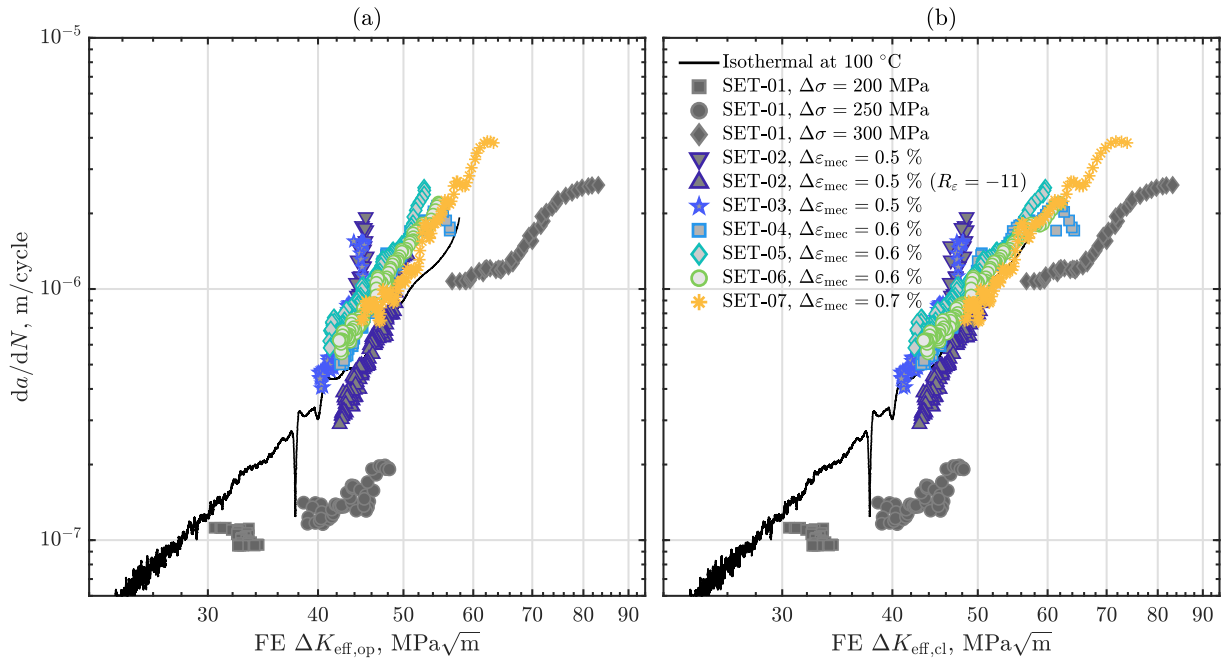


Fig. 17. Crack growth rate versus FE effective stress intensity range using (a) FE effective opening stress intensity range, $FE \Delta K_{eff,op}$; (b) FE effective closing stress intensity range, $FE \Delta K_{eff,cl}$.

lengths are short (in all strain controlled tests, the crack driving force decreases as the crack grows). This suggests that σ_{cl} has more influence on the crack growth behaviour than σ_{op} .

The largest difference between the crack opening and closing stresses, σ_{op} and σ_{cl} , was observed at short crack lengths, see Fig. 9 (b) and Fig. 16. However, this difference decreases as the crack length get longer. The proposed explanation for this behaviour is that, as the crack opens during loading (see Fig. 9 (a)), the crack tip accumulate large local stresses, especially for short cracks in strain controlled tests; during unloading those residual stresses hinders the crack closing process. However, when reaching maximum compression, those stresses at the crack tip relaxes quickly due to the rapid creep rate in this material at 600 °C. Thus, during the next loading, the low residual stresses at the

crack tip requires a higher load level to open the crack. This mismatch between the closing and opening of the crack is also the reason for the hysteresis loop being slightly open, see Fig. 9 (a). The degree of this mismatch reduces with cycles for strain controlled tests (see Fig. 9 (b) and Fig. 16), since the residual stresses reduces with increase in the crack length.

The explanation for the rather large change in the crack closing stress, σ_{cl} , with crack length, a , (see Fig. 16 (b)) can be understood from the $FE \sigma_{nom} - \epsilon_{mec}$ curves shown in Fig. 18. A drop in the maximum nominal stress of the cycle, σ_{max} , can be observed in Fig. 18 at longer crack lengths for all the FE simulated $\Delta \epsilon_{mec}$. This leads to lower local residual stresses at the crack tip, which in-turn reduces the resistance to crack closing (i.e. a drop in σ_{cl}) bringing σ_{cl} closer to σ_{op} as the crack

grows. In addition, the increase in $\Delta\epsilon_{mec}$ can be seen, in Fig. 18, to increase σ_{max} which explains the noticeable distinction of σ_{cl} with different $\Delta\epsilon_{mec}$ (see Fig. 16 (b)). However, the change in crack length has no effect on the minimum nominal stress of the cycle, σ_{min} , explaining the lack of distinction of σ_{op} with different $\Delta\epsilon_{mec}$ (see Fig. 16 (a)). Nevertheless, in the experimental results, σ_{min} increases with time as the crack grows (see Fig. 9 (a)), which explains the discrepancy of the FE crack closure predictions compared to experimental values as the crack length, a , increases (see Fig. 16). This is mainly since higher σ_{max} can be reached if σ_{min} is increasing. Thus, improving the constitutive model to include the change in σ_{min} is considered desirable in future work.

The crack growth behaviour for SET-06, which was cycled prior to pre-cracking, coincides with SET-04 and SET-05 (OP-TMF with $\Delta\epsilon_{mec} = 0.6\%$) as seen in Figs. 10 and 11. This suggest that it does not matter whether or not the crack is present during the inelastic compression in the first half-cycle. Thus, justifying the use of a completely closed sharp crack with contacts conditions to model the first half-cycle (see Fig. 15).

The three-dimensional FE model with a stationary crack and contact conditions (without any node-release or crack growth schemes) was successful in approximating the crack closure stresses obtained from the experimental cycles using the compliance method (see Fig. 16). The FE model incorporated the severe plastic and creep behaviour from the first half-cycle using both elasto-plastic and creep material models for all the simulations. In addition, the relaxation of local stresses was allowed at high temperatures due to the creep model. Any other history dependence effects were not captured by the FE model due to the use of a sharp stationary crack. Both experimentally and numerically computed crack closure stresses were seen to collapse the fatigue crack growth curves together with good agreement, see Figs. 11 and 17.

7. Conclusion

The crack propagation behaviour was investigated for the 9–12 % Cr martensitic steel FB2 which is commonly used at the high-temperature section of steam turbines. The testing was performed under out-of-phase thermomechanical fatigue in both stress and strain control with a temperature range of 100–600 °C. The main conclusions are

- Crack closure was observed for all the tests done in strain control (negative R_e). This was indicated through the change in the global stiffness of specimen below zero nominal stress. A difference was seen between the crack opening stress and the crack closing stress which was more pronounced at short crack lengths and at high mechanical strain ranges.
- Load ratio dependency was observed in the crack growth rate curves when using stress intensity range for only the tensile part of the cycle. By accounting for the crack closure experimentally, i.e. using the effective stress intensity range, the crack growth rates curves collapsed into a single master curve. A better collapse of the curves were seen when using crack closing stress (not crack opening stress). The collapsed curves coincided with an isothermal fatigue crack growth test at 100 °C which suggests that the crack growth rate for FB2 is strongly determined by the minimum temperature of the cycle.
- The crack closure levels were predicted numerically using a three dimensional finite element model with a stationary sharp crack and contact conditions. The finite element effective stress intensity ranges were similar to the experimentally computed.
- The difference between the crack opening and closing stresses was captured and motivated by the finite element modelling. The reduction in the difference between opening and closing stresses with increasing crack length was attributed to the drop in the maximum stress of the cycle, which occurred at lower strain ranges and for long cracks (for strain controlled tests). The maximum stress in the cycle determines the level of the local residual stresses introduced at the crack tip. Large residual stresses would hinder crack

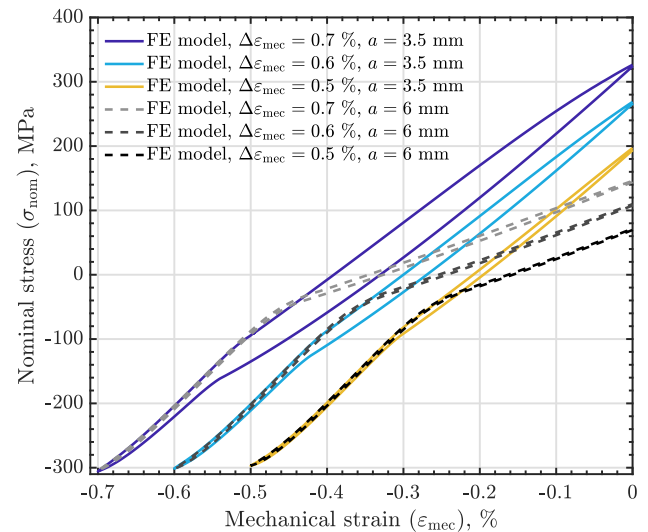


Fig. 18. Finite element obtained $\sigma_{nom}-\epsilon_{mec}$ curves for three different mechanical strain ranges, $\Delta\epsilon_{mec}$, and two different crack lengths, a . All curves were taken from the 5th FE cycle.

closing process but relax at the minimum stress of the cycle (due to the creep behaviour of the material at the maximum temperature of 600 °C) creating the mismatch with the crack opening stress.

Declaration of Competing Interest

The authors declare that they have no known competing financial interests or personal relationships that could have appeared to influence the work reported in this paper.

Acknowledgement

This project has received funding from the European Union's Horizon 2020 research and innovation programme under grant agreement No. 764545. Siemens AG is acknowledged for their support and for providing the material used in the testing.

References

- [1] Ferruzza D, Topel M, Laumert B, Haglind F. Impact of steam generator start-up limitations on the performance of a parabolic trough solar power plant. *Sol Energy* 2018;169:255–63.
- [2] Topel M, Guédez R, Laumert B. Impact of increasing steam turbine flexibility on the annual performance of a direct steam generation tower power plant. *Energy Procedia* 2015;69:1171–80. Int Conf on Concentrating Solar Power and Chemical Energy Systems, SolarPACES 2014.
- [3] Steam Turbines for Flexible Load Operation in the Future Market of Power Generation, volume 6: Oil and Gas Applications; Concentrating Solar Power Plants; Steam Turbines; Wind Energy of Turbo Expo: Power for Land, Sea, and Air, 2012. <https://doi.org/10.1115/GT2012-69312>.
- [4] Stekovic S, Jones J, Engel B, Whittaker M, Norman V, Rouse J, et al. Devtmf â€” towards code of practice for thermo-mechanical fatigue crack growth. *Int J Fatigue* 2020;138:105675.
- [5] Palmer J, Jones J, Dyer A, Smith R, Lancaster R, Whittaker M. Development of test facilities for thermo-mechanical fatigue testing. *Int J Fatigue* 2019;121:208–18.
- [6] Jacques S, Lynch M, Wisbey A, Stekovic S, Williams S. Development of fatigue crack growth testing under thermo-mechanical fatigue conditions. *Mater High Temp* 2013;30:49–61.
- [7] Loureiro-Homs J, Almroth P, Palmert F, Gustafsson D, Simonsson K, Eriksson R, et al. Accounting for crack closure effects in tmf crack growth tests with extended hold times in gas turbine blade alloys. *Int J Fatigue* 2021;142:105917.
- [8] Wolf E. Fatigue crack closure under cyclic tension. *Eng Fract Mech* 1970;2:37–45.
- [9] Jacobsson L, Persson C, Melin S. Thermo-mechanical fatigue crack propagation experiments in inconel 718. *Int J Fatigue* 2009;31:1318–26.
- [10] Almroth P, Gustafsson D, Loureiro Homs J, Simonsson K. Out-of-phase thermo-mechanical fatigue crack growth and the effect of the compressive minimum load level on crack closure at notches. *Int J Fatigue* 2020;141:105906.

- [11] Dai J, Marchand NJ, Hongoh M. Thermal Mechanical Fatigue Crack Growth in Titanium Alloys: Experiments and Modelling, ASTM International, West Conshohocken, PA 1996:187–209. <https://doi.org/10.1520/STP16454S>.
- [12] Palmert F, Moverare J, Gustafsson D. Thermomechanical fatigue crack growth in a single crystal nickel base superalloy. *Int J Fatigue* 2019;122:184–98.
- [13] Ilg W, Mcevely AJ. The rate of fatigue-crack propagation for two aluminum alloys under completely reversed loading. NASA Technical Note D-52. Langley Research Center, Langley Field, Va, 1959. URL: <https://hdl.handle.net/2027/uiug.30112106741124>.
- [14] McClung R, Sehitoglu H. On the finite element analysis of fatigue crack closure-2. numerical results. *Eng Fract Mech* 1989;33:253–72.
- [15] Loureiro-Homs J, Gustafsson D, Almroth P, Simonsson K, Eriksson R, Leidermark D. Accounting for initial plastic deformation for fatigue crack growth predictions under tmf loading condition. *Int J Fatigue* 2020;136:105569.
- [16] Kern T-U, Staubli M, Scarlin B. The European Efforts in Material Development for 650°C USC Power Plants - COST 522. *ISIJ Int* 2002;42:1515–9.
- [17] Azeez A, Eriksson R, Leidermark D, Calmunger M. Low cycle fatigue life modelling using finite element strain range partitioning for a steam turbine rotor steel. *Theor Appl Fract Mech* 2020;107:102510.
- [18] Kern TU, Mayer KH, Donth B, Zeiler G, Di Gianfrancesco A. The european efforts in development of new high temperature rotor materials - cost536. In: Proc. of 9th Liege Conf. on Materials for Advanced Power Engineering, Liege, Belgium, 2010, p. 27–36.
- [19] Abe F. Research and Development of Heat-Resistant Materials for Advanced USC Power Plants with Steam Temperatures of 700 Å°C and Above. *Engineering* 2015;1:211–24.
- [20] Holdsworth S. Creep resistant materials for steam turbines. In: Reference Module in Materials Science and Materials Engineering. Elsevier; 2016. <https://doi.org/10.1016/B978-0-12-803581-8.02063-4>.
- [21] Zeiler G. 6 - martensitic steels for rotors in ultra-supercritical power plants. In: Di Gianfrancesco A. editor. *Materials for Ultra-Supercritical and Advanced Ultra-Supercritical Power Plants*, Woodhead Publishing, 2017, p. 143–174. <https://doi.org/10.1016/B978-0-08-100552-1.00006-3>.
- [22] ASTM E1457-07, Standard Test Method for Measurement of Creep Crack Growth Times in Metals, Standard, ASTM International, West Conshohocken, PA, 2007. <http://doi.org/10.1520/E1457-07>.
- [23] ISO 12108:2002(E), Metallic materials — Fatigue testing — Fatigue crack growth method, Standard, International Organization for Standardization, Geneva, CH, 2002.
- [24] ISO 12111:2011(E), Metallic materials—Fatigue testing—Strain-controlled thermomechanical fatigue testing method, Standard, International Organization for Standardization, Geneva, CH, 2011.
- [25] ASTM E2368-10, Standard Practice for Strain Controlled Thermomechanical Fatigue Testing, Standard, ASTM International, West Conshohocken, PA, 2017. <http://doi.org/10.1520/E2368-10R17>.
- [26] Ewest D, Almroth P, Sjödin B, Simonsson K, Leidermark D, Moverare J. A modified compliance method for fatigue crack propagation applied on a single edge notch specimen. *Int J Fatigue* 2016;92:61–70.
- [27] Norman V, Stekovic S, Jones J, Whittaker M, Grant B. On the mechanistic difference between in-phase and out-of-phase thermo-mechanical fatigue crack growth. *Int J Fatigue* 2020;135:105528.
- [28] ASTM E647-13a, Standard Test Method for Measurement of Fatigue Crack Growth Rates, Standard, ASTM International, West Conshohocken, PA, 2013. <http://doi.org/10.1520/E0647-13A>.
- [29] ABAQUS User's Manual, Version 2017, Dassault Systemes, Johnston, RI, USA, 2017.
- [30] FRANC3D 7.3.4, Fracture Analysis Consultants, Inc, Ithaca, NY, USA, 2019. URL: <http://www.fracanalysis.com/software.html>.
- [31] MathWorks, MATLAB Documentation (R2019a), 2019.
- [32] Paris P, Erdogan F. A Critical Analysis of Crack Propagation Laws. *J Basic Eng* 1963;85:528–33.
- [33] Hosford WF. Mechanical Behavior of Materials, 2 ed., Cambridge University Press, 2009. <http://doi.org/10.1017/CBO9780511810923>.